

JYX



This is a self-archived version of an original article. This version may differ from the original in pagination and typographic details.

Author(s): The NEMO-3 Collaboration

Title: Search for periodic modulations of the rate of double- β decay of Mo100 in the NEMO-3 detector

Year: 2021

Version: Published version

Copyright: © 2021 American Physical Society

Rights: In Copyright

Rights url: <http://rightsstatements.org/page/InC/1.0/?language=en>

Please cite the original version:

The NEMO-3 Collaboration. (2021). Search for periodic modulations of the rate of double- β decay of Mo100 in the NEMO-3 detector. *Physical Review C*, 104(6), Article L061601.
<https://doi.org/10.1103/PhysRevC.104.L061601>

Search for periodic modulations of the rate of double- β decay of ^{100}Mo in the NEMO-3 detector

R. Arnold,¹ C. Augier,² A. S. Barabash,³ A. Basharina-Freshville,⁴ S. Blondel,² S. Blot,⁵ M. Bongrand,² D. Bourssette,² R. Breier,⁶ V. Brudanin,^{7,8} J. Busto,⁹ A. J. Caffrey,¹⁰ S. Calvez,² C. Cerna,¹¹ J. P. Cesar,¹² M. Ceschia,⁴ A. Chapon,¹³ E. Chauveau,¹¹ A. Chopra,⁴ L. Dawson,⁴ D. Duchesneau,¹⁴ D. Durand,¹³ G. Eurin,^{2,4} J. J. Evans,⁵ L. Fajt,¹⁵ D. Filosofov,⁷ R. Flack,⁴ P. Franchini,¹⁶ X. Garrido,² C. Girard-Carillo,² H. Gómez,² B. Guillon,¹³ P. Guzowski,⁵ R. Hodák,¹⁵ A. Huber,¹¹ P. Hubert,¹¹ C. Hugon,¹¹ M. H. Hussain,⁴ S. Jullian,² A. Klimenko,⁷ O. Kochetov,⁷ S. I. Konovalov,³ V. Kovalenko,⁷ D. Lalanne,² K. Lang,¹² Y. Lemièrre,¹³ T. Le Noblet,¹⁴ Z. Liptak,¹² X. R. Liu,⁴ P. Loaiza,² G. Lutter,¹¹ M. Macko,¹⁵ C. Macolino,² F. Mamedov,¹⁵ C. Marquet,¹¹ F. Mauger,¹³ A. Minotti,¹⁴ B. Morgan,¹⁷ J. Mott,⁴ I. Nemchenok,⁷ M. Nomachi,¹⁸ F. Nova,¹² F. Nowacki,¹ H. Ohsumi,¹⁹ G. Oliviero,¹³ R. B. Pahlka,¹² V. Palusova,^{11,6} C. Patrick,⁴ F. Perrot,¹¹ A. Pin,¹¹ F. Piquemal,^{11,20} P. Povinec,⁶ P. Přidal,¹⁵ W. S. Quinn,⁴ Y. A. Ramachers,¹⁷ A. Remoto,¹⁴ J. L. Reyss,²¹ C. L. Riddle,¹⁰ E. Rukhadze,¹⁵ R. Saakyan,⁴ A. Salamatin,⁷ R. Salazar,¹² X. Sarazin,² J. Sedgbeer,¹⁶ Yu. Shitov,^{7,16} L. Simard,^{2,22} F. Šimkovic,⁶ A. Smetana,¹⁵ A. Smolnikov,⁷ S. Söldner-Rembold,⁵ B. Soulé,¹¹ I. Štekl,¹⁵ J. Suhonen,²³ C. S. Sutton,²⁴ G. Szklarz,² H. Tedjditi,⁹ J. Thomas,⁴ V. Timkin,⁷ S. Torre,⁴ Vl. I. Tretyak,²⁵ V. I. Tretyak,⁷ V. I. Umatov,³ I. Vanushin,³ C. Vilela,⁴ V. Vorobel,²⁶ D. Waters,⁴ and F. Xie⁴

(The NEMO-3 Collaboration)

¹*IPHC, ULP, CNRS/IN2P3, F-67037 Strasbourg, France*

²*LAL, Université Paris-Sud, CNRS/IN2P3, Université Paris-Saclay, F-91405 Orsay, France*

³*NRC “Kurchatov Institute,” ITEP, 117218 Moscow, Russia*

⁴*UCL, London WC1E 6BT, United Kingdom*

⁵*University of Manchester, Manchester M13 9PL, United Kingdom*

⁶*FMFI, Comenius University, SK-842 48 Bratislava, Slovakia*

⁷*JINR, 141980 Dubna, Russia*

⁸*National Research Nuclear University MEPhI, 115409 Moscow, Russia*

⁹*Aix Marseille Université, CNRS, CPPM, F-13288 Marseille, France*

¹⁰*Idaho National Laboratory, Idaho Falls, Idaho 83415, USA*

¹¹*Université de Bordeaux, CNRS, CENBG, UMR 5797, F-33170 Gradignan, France*

¹²*University of Texas at Austin, Austin, Texas 78712, USA*

¹³*LPC Caen, ENSICAEN, Université de Caen, CNRS/IN2P3, F-14050 Caen, France*

¹⁴*LAPP, Université de Savoie, CNRS/IN2P3, F-74941 Annecy-le-Vieux, France*

¹⁵*Institute of Experimental and Applied Physics, Czech Technical University in Prague, CZ-11000 Prague, Czech Republic*

¹⁶*Imperial College London, London SW7 2AZ, United Kingdom*

¹⁷*University of Warwick, Coventry CV4 7AL, United Kingdom*

¹⁸*Osaka University, 1-1 Machikaneyama Toyonaka, Osaka 560-0043, Japan*

¹⁹*Saga University, Saga 840-8502, Japan*

²⁰*Laboratoire Souterrain de Modane, F-73500 Modane, France*

²¹*LSCE, CNRS, F-91190 Gif-sur-Yvette, France*

²²*Institut Universitaire de France, F-75005 Paris, France*

²³*Jyväskylä University, FIN-40351 Jyväskylä, Finland*

²⁴*MHC, South Hadley, Massachusetts 01075, USA*

²⁵*Institute for Nuclear Research, 03028, Kyiv, Ukraine*

²⁶*Charles University, Faculty of Mathematics and Physics, CZ-12116 Prague, Czech Republic*



(Received 23 November 2020; revised 17 March 2021; accepted 28 September 2021; published 8 December 2021)

Double-beta decays of ^{100}Mo from the 6.0195-year exposure of a 6.914 kg high-purity sample were recorded by the NEMO-3 experiment that searched for neutrinoless double-beta decays. These ultrarare transitions to ^{100}Ru have a half-life of approximately 7×10^{18} years and have been used to conduct the first-ever search for periodic variations of this decay mode. The Lomb-Scargle periodogram technique, and its error-weighted extension, were employed to look for periodic modulations of the half-life. Data show no evidence at the 95% confidence level of modulations with amplitude greater than 2.5% in the frequency range of 0.33225 yr^{-1} to 360 yr^{-1} .

DOI: [10.1103/PhysRevC.104.L061601](https://doi.org/10.1103/PhysRevC.104.L061601)

Introduction. The invariance of fundamental constants of nature has been scrutinized in a broad range of physics contexts including considerations discussed by Milne [1], Walker [2], Dirac [3,4], Chandrasekhar [5], and Kothari [6] during the initial ascent of data-based cosmology of the expanding Universe. Modern cosmology and the observed evolution of the Universe are closely related to properties of interactions of elementary particles, and impose tight bounds on possible changes in constants that include the strength of gauge couplings as a function of time elapsed since the Big Bang. A number of authors studied these constraints and their implications, see, e.g., Refs. [7–16]. Many theoretical ideas and implied phenomena are discussed in the literature and have been reported in reviews [17,18] that also contain exhaustive lists of references on this subject.

Closely related to the time invariance of physical constants is their periodicity, given the ubiquitous presence of cyclic processes in nature at almost all distance and timescales. There are ongoing searches and tests of such phenomena, mostly but not only connected to dark matter and dark energy [19–21]. Relevant to the study presented here are results of *a posteriori* data analyses of measurements of nuclear decay half-lives which have yielded unexpected periodicities, including annual modulations that authors have linked to the periodicity of the Earth-Sun distance and solar activity [22–33]. However, other analyses of the same data do not reveal any significant modulations [34–36].

Difficulties with precision testing the time variation of half-lives of long-lived radioisotopes can be attributed, in part, to two important factors: the time duration of measurements, and the necessity of long-term control of background phenomena, which often exhibit time and/or seasonal periodicities. Examples of such phenomena include the average environmental temperature; radon levels in the ground, buildings, and caverns; the seasonal cosmic-ray flux modulation; the solar wind intensity related to the Earth-Sun distance; the phase of the lunar cycle and tides, and solar activity.

In this Letter, we report results of a search for periodicity of double-beta ($\beta\beta$) decays of $^{100}\text{Mo} \rightarrow ^{100}\text{Ru}$. Data were collected over a period of approximately eight years by the NEMO-3 experiment [37,38]. The experiment, designed to search for neutrinoless double beta decay ($0\nu\beta\beta$), had an exquisite capability of background identification and suppression. NEMO-3 collected an unprecedentedly large data set of two-neutrino $\beta\beta$ decays ($2\nu\beta\beta$). These extremely rare events with two electrons in the final state of the ^{100}Mo decay, whose half-life is about 7×10^{18} years, served as a unique testing ground for the first-ever search for periodicity of a second-order weak transition on timescales shorter than or comparable to the measuring period.

The NEMO-3 Experiment. The NEMO-3 detector [39] was designed to detect two electrons in the final state of neutrinoless $\beta\beta$ decays. Thin foils of the source isotopes were surrounded by a tracking chamber and plastic calorimeter blocks that reconstructed the full kinematics of various decays and interactions within the detector. The source foils were strips about 65 mm wide, 2480 mm long, and 40–60 mg/cm² thick and were made of various $\beta\beta$ decay isotopes (^{100}Mo , ^{82}Se , ^{130}Te , ^{116}Cd , ^{150}Nd , ^{96}Zr , and ^{48}Ca) totaling about 10 kg.

These foil strips were arranged vertically to form a cylinder such that the tracking and calorimetric volumes on either side formed a toroidal geometry for the whole detector. For the purposes of this analysis, only events from the ^{100}Mo foils were considered. This particular isotope constituted the majority, 6.914 kg, of the total source mass in NEMO-3. The tracking volume that surrounded either side of the foils was comprised of 6180 drift wire cells, operating in Geiger mode, within a gas mixture of helium-argon (95%–1%), and ethanol with water vapor (4%). The tracking volume was then further enclosed by the calorimeter walls composed of 1940 plastic scintillator blocks coupled to photomultiplier tubes. Finally, a large solenoid encircled the detector to produce a 25 G magnetic field to help with e^+/e^- discrimination. The entire detector was shielded from external backgrounds by a combination of iron, wood, paraffin, and borated water. The detector was placed in the Modane Underground Laboratory in the Fréjus tunnel in the Alps which provided 4800 m.w.e. overburden to shield from cosmic rays.

The detector was operated from early 2003 until early 2011 with data-taking split into two run periods known as Phase 1 (February 2003 to September 2004) and Phase 2 (October 2004 to January 2011). During Phase 2, an additional enclosure was installed, surrounding the detector. Filled with radon-filtered air, this enclosure greatly reduced radon permeation into the detector resulting in a significant increase in the purity of the signal channel for Phase 2. Only these lower background runs were considered for the final analysis presented herein. The total span of the runs from this period amounts to 6.0195 y.

Event Selection. The purpose of this analysis was to search for periodic trends in the rate of $\beta\beta$ decays (with no distinction between $2\nu\beta\beta$ and theoretical $0\nu\beta\beta$ decays) originating in the ^{100}Mo source foils, which required counting the number of such decays per unit time recorded in the NEMO-3 detector. Data taking was divided into specific run periods with durations ranging from tens of minutes to just over two days. The ^{100}Mo activity yielding $\beta\beta$ events was about 0.1 Bq and, since most runs lasted longer than 20 minutes, most of them accumulated over 100 $\beta\beta$ events. A discrete time series of the decay rate was constructed by taking the number of selected events in a run divided by the duration of the run to yield a value for the observed rate. The average $\beta\beta$ event rate for each run was associated with a timestamp, corresponding to the midpoint of the run.

Events that were selected for inclusion into this calculation were chosen based on a wide range of criteria to minimize the contribution from background processes which could mimic topologies of a $\beta\beta$ decay. The primary characteristics of a $\beta\beta$ decay event are the identification of two tracks with curvatures consistent with negatively charged particles, with common origins in the ^{100}Mo foil supported by time-of-flight measurements and geometric extrapolation, and with associated energy deposits in scintillator blocks; also with no coincident alpha particles (short straight tracks); and no gamma particles (unassociated scintillator hits) with energy deposits greater than or equal to 150 keV.

The resultant sample had a very high purity (a very similar event selection resulted in a signal to background ratio of

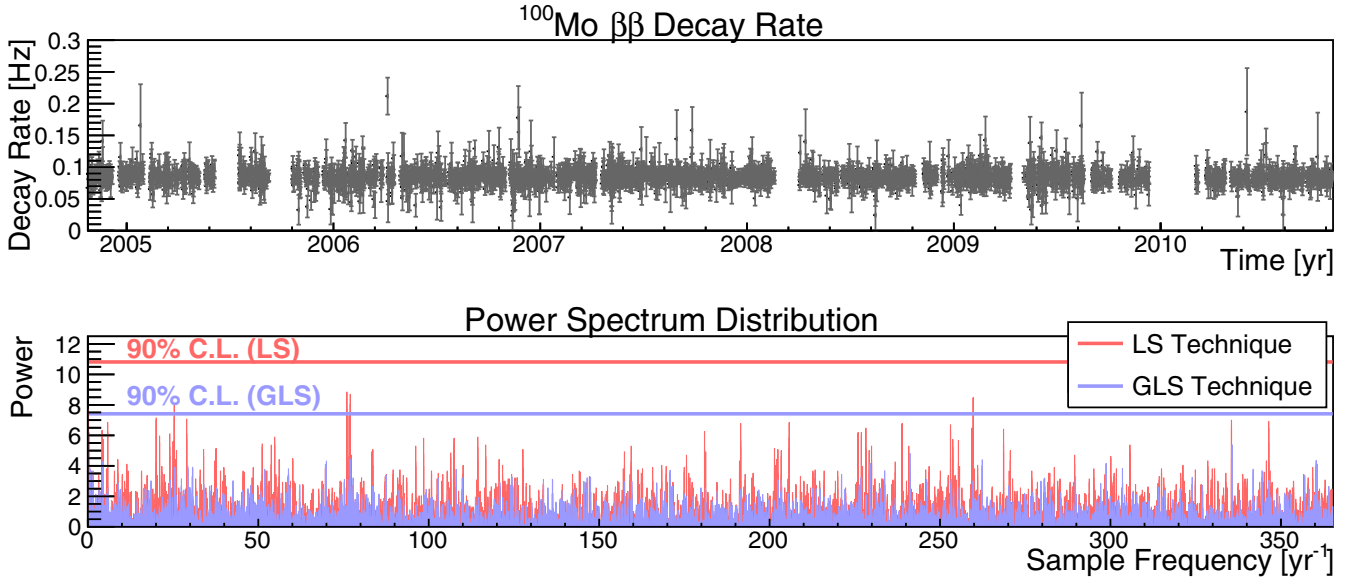


FIG. 1. Results of applying both of the periodogram techniques to the $\beta\beta$ decay rate time series of Phase 2 ^{100}Mo data. The upper plot shows the efficiency-corrected time series that was analyzed. The lower plot shows the periodograms obtained from applying the LS and GLS techniques. The horizontal lines denote the threshold powers, in each technique, for reaching a 90% confidence level based on the “shuffle test” method described in “Significance and Sensitivity Studies”.

76 [40]) and no background subtraction was performed in calculating per-run event rates. The possibility of time varying backgrounds was also considered, in particular due to the potential seasonal variation of radon levels. No modulations appeared in the analysis, of either the Phase 1 or Phase 2 data, at frequencies corresponding to such processes.

The decay rate based on the raw number of events that passed these selection requirements had to be corrected by the efficiency of the detector during each run period. This correction scaling could vary from one run to the next and was accounted for using precise and comprehensive Monte Carlo simulations of the NEMO-3 experiment. The data yielded an average per-run rate of 3.9 mHz with a standard deviation of 0.52 mHz. The average run was 8.3 hours in duration (standard deviation of 4.7 hours) and saw approximately 115.9 events in that time (standard deviation of 66.7 events). In total, 449 733 events were collected, with a mean efficiency of 4.6% (standard deviation of 0.34), across the 3869 run periods. After scaling for this efficiency on a per-run basis, the resultant decay rate time series is shown in Fig. 1. A study of the most significant systematic errors showed that their contributions were small compared with statistical fluctuations from one run to the next.

The Search for Periodicities. Periodic trends in data can be identified by constructing a power spectrum, or periodogram, for a range of frequencies. Two related approaches are used here in order to both compare with other analyses and cross-check the conclusions: the more commonly used Lomb-Scargle (LS) [41,42] method which is used on unevenly sampled data, and the Generalized LS (GLS) [43] method which allows data to be weighted and accounts for an overall offset term.

Periodogram analyses, which are commonplace in astronomy and astrophysics, have also seen use in the fields of

nuclear and particle physics. For example, see Refs. [25–28] and [33]. Of particular note are searches for periodic variations in neutrino fluxes across different experiments, see e.g., Refs. [44–49], and, more recently, Refs. [36,50,51].

For a discrete time series $X(t_j)$ consisting of N entries, the basic Lomb-Scargle power, $P_{\text{LS}}(\omega)$ can be calculated at a given sample frequency f (where $\omega = 2\pi f$) by

$$P_{\text{LS}}(\omega) = \frac{1}{2\sigma^2} \left\{ \frac{(\sum_{j=1}^N [X(t_j) - \bar{X}] \cos[\omega(t_j - \tau)])^2}{\sum_{j=1}^N \cos^2[\omega(t_j - \tau)]} + \frac{(\sum_{j=1}^N [X(t_j) - \bar{X}] \sin[\omega(t_j - \tau)])^2}{\sum_{j=1}^N \sin^2[\omega(t_j - \tau)]} \right\}, \quad (1)$$

where \bar{X} is the mean of the data points, σ is their standard deviation, and τ is defined by the relation $\tan(2\omega\tau) = \sum_{j=1}^N \sin(2\omega t_j) / \sum_{j=1}^N \cos(2\omega t_j)$. The periodogram is constructed by calculating this power over a range of frequencies of interest.

A well-known property of the LS technique is its equivalence to least-squares fitting of sine waves [42]. By taking into account an offset term and weights, the GLS technique extends this equivalence to a full χ^2 fitting approach. The end result is a new expression for the Generalized Lomb-Scargle power, $P_{\text{GLS}}(\omega)$, given by

$$P_{\text{GLS}}(\omega) = \frac{1}{XX \cdot D} [SS \cdot (XC)^2 + CC \cdot (XS)^2 - 2CS \cdot XC \cdot XS], \quad (2)$$

where $D = CC \cdot SS - (CS)^2$ and the following abbreviations are used [with summations running over the same indices as

in Eq. (1)]:

$$\begin{aligned}
 XX &= \sum w_j [X(t_j) - \bar{X}]^2, \\
 XC &= \sum w_j [X(t_j) - \bar{X}] \cos(\omega t_j), \\
 XS &= \sum w_j [X(t_j) - \bar{X}] \sin(\omega t_j), \\
 CC &= \sum w_j \cos^2(\omega t_j) - \left[\sum w_j \cos(\omega t_j) \right]^2, \\
 SS &= \sum w_j \sin^2(\omega t_j) - \left[\sum w_j \sin(\omega t_j) \right]^2, \\
 CS &= \sum w_j \cos(\omega t_j) \sin(\omega t_j) \\
 &\quad - \left[\sum w_j \cos(\omega t_j) \sum w_j \sin(\omega t_j) \right].
 \end{aligned}$$

Here the w_j are the weights for each $X(t_j)$, given by $w_j = \frac{1}{W} \frac{1}{\sigma_j}$ for $W = \sum \frac{1}{\sigma_j}$ where the σ_j are the errors, and so the mean is now $\bar{X} = \sum w_j X(t_j)$. Another known feature of (G)LS periodograms is that, if the time series $X(t_j)$ is made up of Gaussian random values with no underlying modulation, then the resultant powers should be exponentially distributed with unit mean [42]. The false alarm probability (FAP) of finding a power larger than P is found via the expression

$$\text{FAP}(P) = 1 - (1 - e^{-P})^M, \quad (3)$$

where the power M , equal to the number of frequencies sampled, acts as a statistical penalty to mitigate the increased chance of finding spurious large peaks due to the sheer size of the sample space. This allows a confidence level (CL) value to be calculated for a given power:

$$\text{CL}(P) = (1 - e^{-P})^M \times 100\%. \quad (4)$$

The resultant significance of periodogram peaks depends critically on the initial assumption of the Gaussian distribution of the data points. The GLS periodogram expression given in Eq. (2) also requires a normalization factor [43] in order for Eq. (4) to apply and the normalization scheme proposed by Baluev [52] was used. However, the most reliable way to assess the significance of periodogram peaks is via statistical methods, which are described in ‘‘Significance and Sensitivity Studies’’. The simple but rough significance approximation obtained from Eq. (4) was thus employed for sensitivity studies which were optimized to reduce computational loads.

It should be stated that all the analysis reported was first developed on the Phase 1 data in order to carry out a blind analysis which was then applied to the Phase 2 data, which were used to extract the final result.

The Phase 2 data series contained 3869 runs and for creating the periodogram, an oversampling factor of two was used. This meant that 7738 frequencies, twice the number of data points, were sampled. These frequencies were evenly distributed in the range $[0.33225, 365.25] \text{ yr}^{-1}$ which was chosen based on the maximum and minimum modulation periods that could be detectable within the given duration of data taking. The minimum period was limited by the average run spacing ΔT_{avg} such that $f_{\text{max}} = 1/(2 \times \Delta T_{\text{avg}})$. A

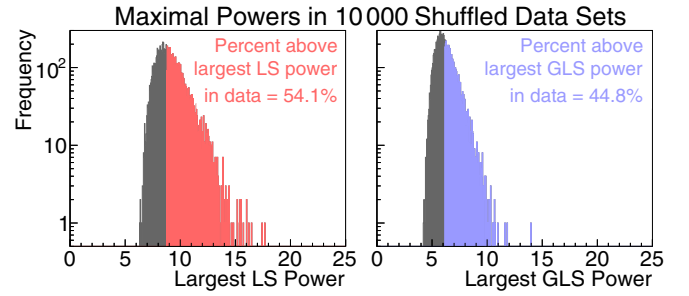


FIG. 2. A distribution of the maximal LS (left) and GLS (right) powers in 10 000 randomly shuffled null-hypothesis data sets (no applied modulations). These distributions are used to calculate the 90% CL lines in Fig. 1.

conservative value of 12 hours was used for the average run spacing which translates to a minimum period of one day or $f_{\text{max}} = 365.25 \text{ yr}^{-1}$. Similarly, the maximum period was determined by the total span of the data such that at least two full periods of a modulation were contained in the data. This implies that $f_{\text{min}} = 2/(\text{span}) = 0.33225 \text{ yr}^{-1}$. The resultant LS and GLS periodograms are shown in the lower plot of Fig. 1.

The largest and therefore most significant LS power of 8.78 was found at the frequency of 76.26 yr^{-1} , corresponding to a periodicity of approximately 4.8 days, while the largest GLS power of 6.16 was found at the frequency of 0.47 yr^{-1} , corresponding to a periodicity of approximately 777 days or 2.1 years. The fact that the locations of these peaks disagreed between the two techniques and that neither had any correlation with periodicities found in any of the previously mentioned references indicates they are very likely random fluctuations.

Significance and Sensitivity Studies. The significance of the periodogram peaks was calculated by testing how often a specific power was exceeded in many similar time series comprised of randomized pseudodata with no modulation. Such pseudodata sets were created from the Phase 2 data by randomizing, 10 000 times, the mapping of rate values and uncertainties to associated runtimes. This procedure destroyed any temporal dependencies and preserved the structure of the original data in terms of the actual values and their associated errors as well as their temporal spacing. This is called the ‘‘shuffle test’’ [53]. The LS and GLS techniques were then applied to each of these 10 000 new time series and the largest powers were recorded for each resultant periodogram. The largest powers from the true data could then be compared against these maximal powers from the pseudodata to estimate their significance. The results are shown in Fig. 2 where the division in each distribution shows what percentage of maximal powers lie above the largest power found in the data. For the LS (GLS) technique where the largest power was 8.78 (6.16), a larger power was found in the randomized pseudodata sets 54.1% (44.8%) of the time.

Further studies with these pseudodata sets were also undertaken to estimate the sensitivity of the data to detecting different modulations. To do this, a modulation to the

TABLE I. A Summary of amplitude and frequency values used for the injected modulations to test detection sensitivity.

	Amplitude (A) [%]	Step size (ΔA) [%]
	0.5–4	0.1
Range	Freq. (f) [yr^{-1}]	Step size (Δf) [yr^{-1}]
Low	0.03–0.1	0.005
Mid	0.15–2	0.05
High	15–360	15

pseudodata sets was applied in the form of

$$R(t_i) = N[1 + A \sin(2\pi f t_i + \phi)], \quad (5)$$

where N is a normalization constant to match the mean of the unmodulated data, A represents a fractional or relative amplitude (which will be denoted as a percentage relative to the mean rate) for the applied modulation, f is the frequency of the applied modulation, and ϕ is the modulation phase.

Although the final analysis only sampled frequencies corresponding to modulations in which at least two full periods are present in the data, the sensitivity studies sampled down to even smaller frequencies. This helped determine an appropriate lower bound and allowed for the study of the behavior of the two techniques in the low-frequency domain. Due to the computationally intensive nature of these studies, the sample frequency range was broken down into three regimes (low, mid, and high) that included different spacing between frequencies to limit the total number of trials that were needed. A summary of the various amplitudes and frequencies that were used for the injected modulations are shown in Table I. It should be noted that, due to these computational efficiency

needs, the final results statement can only be applied to a maximum frequency range up to 360 yr^{-1} .

For each point in this amplitude-frequency phase space 100 different pseudodata sets were analyzed to average out random variations. At each combination of modulation amplitude and frequency, the LS and GLS periodograms were constructed and the average (across all 100 sets) of the largest power was recorded, as well as its estimated CL value derived from Eq. (4). This was used to create a contour plot of CL values in the modulation-amplitude frequency space. These are shown in Fig. 3 for the three frequency regimes and with the input modulation phase set to zero.

The results showed that for mid and high ranges of modulation frequencies, the detection sensitivity only depended on the input modulation amplitudes. In these two regimes, any applied modulation of amplitude greater than or equal to 2% (2.5%) was detected at the 95% CL or higher using the LS (GLS) technique, regardless of the frequency. In the low-frequency regime, where modulation periods varied between 10–33 years, larger amplitudes were generally required before being detected at 95% CL. Here there was also a dependence on both the input frequency and the phase value. This is because only partial wave forms were being captured in the pseudodata and if a more linear slice of the waveform was observed, the sensitivity was reduced compared with other values of input frequency and phase.

Summary and Conclusions. A power spectrum analysis was used to search for temporal variations of the second-order weak process of $\beta\beta$ decay, in the highly pure sample of $6.0195 \text{ y }^{100}\text{Mo}$ decay events in the NEMO-3 detector. The analyzed data set was sensitive to modulations with periods between one day and three years.

Power spectra consistent with the null hypothesis were obtained for an amplitude of greater than 2.0% (2.5%) at 95%

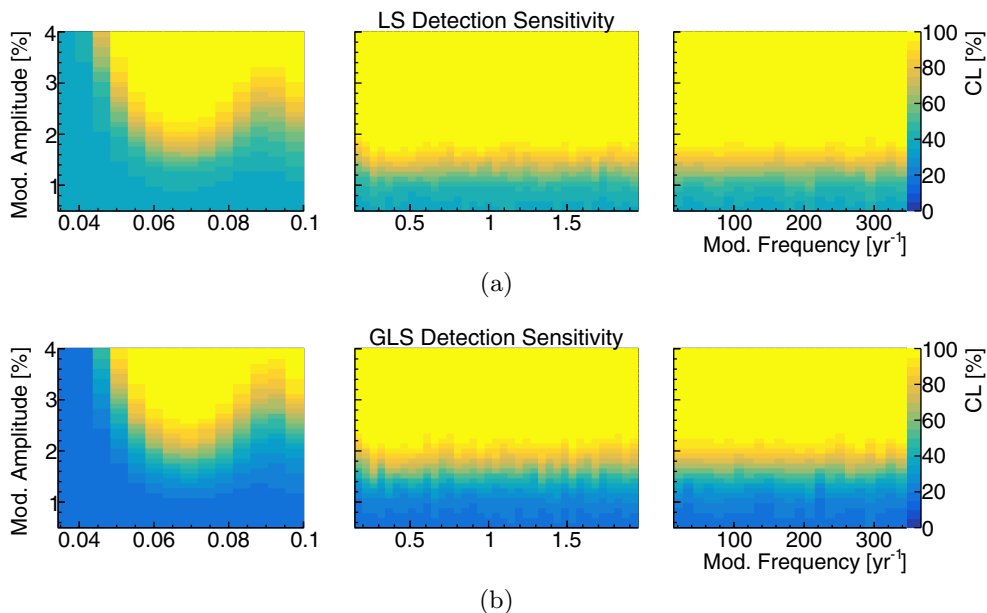


FIG. 3. (a) LS and (b) GLS detection sensitivity as a function of modulation parameters A and f ($\phi = 0$) in three frequency regimes: low, mid, and high. The z axis, color, at each point denotes the estimated CL value of the largest peak, averaged over 100 periodograms.

CL in the frequency range from $0.33225\text{--}360\text{ yr}^{-1}$ using the LS (GLS) method. Of particular interest are frequencies of order 1 yr^{-1} relating to the Earth's orbital period and those in the range $10\text{--}15\text{ yr}^{-1}$ relating to solar synodic rotation rates [22–33].

This result can be translated into a limit on the temporal stability of the weak coupling constant G_F . The $\beta\beta$ decay lifetime is proportional to G_F^4 and so a 2% change in the lifetime would correspond to a 0.5% change in the value of G_F . While claims of modulations in single-beta decays were on the order of 0.1% [23], corresponding to potential changes in G_F of 0.05% (owing to a proportionality to the second power),

the constraint presented herein represents a result very robust against environmental effects owing to the event selection criteria, and therefore quite different systematics from that of other measurements. It is the first-ever such limit achieved measuring the second-order weak process of $\beta\beta$ decay.

Acknowledgments. We thank the staff of the Modane Underground Laboratory for their technical assistance in running the experiment. We acknowledge support by the grant agencies of the Czech Republic, CNRS/IN2P3 in France, RFBR in Russia (NCNIL No19-52-16002), APVV in Slovakia, the Science and Technology Facilities Council, part of U.K. Research and Innovation, and the NSF in the USA.

-
- [1] E. A. Milne, *Proc. R. Soc. London, Ser. A* **158**, 324 (1937).
 [2] A. G. Walker, *Proc. London Math. Soc.* **s2-42**, 90 (1937).
 [3] P. A. M. Dirac, *Nature (London)* **139**, 323 (1937).
 [4] P. A. M. Dirac, *Proc. R. Soc. London, Ser. A* **165**, 199 (1938).
 [5] S. Chandrasekhar, *Nature (London)* **139**, 757 (1937).
 [6] D. S. Kothari, *Nature (London)* **142**, 354 (1938).
 [7] S. Weinberg, *Phil. Trans. R. Soc. London A* **310**, 249 (1983).
 [8] S. Weinberg, *Phys. Lett. B* **125**, 265 (1983).
 [9] E. W. Kolb, M. J. Perry, and T. P. Walker, *Phys. Rev. D* **33**, 869 (1986).
 [10] J. Preskill, *Nucl. Phys. B* **323**, 141 (1989).
 [11] K. A. Olive, M. Pospelov, Y. Z. Qian, A. Coc, M. Casse, and E. Vangioni-Flam, *Phys. Rev. D* **66**, 045022 (2002).
 [12] K. A. Olive, *Can. J. Phys.* **89**, 361 (2011).
 [13] J. P. Uzan, *C. R. Phys.* **16**, 576 (2015).
 [14] H. Fritzsch, J. Solà, and R. C. Nunes, *Eur. Phys. J. C* **77**, 193 (2017).
 [15] A. Braconi, M. C. Chen, and G. Gaswint, *Phys. Rev. D* **100**, 015032 (2019).
 [16] A. Balcerzak and K. Marosek, *Eur. Phys. J. C* **79**, 563 (2019).
 [17] J. P. Uzan, *Living Rev. Relativ.* **14**, 2 (2011).
 [18] C. J. A. P. Martins, *Rep. Prog. Phys.* **80**, 126902 (2017).
 [19] J. D. Lewin and P. F. Smith, *Astropart. Phys.* **6**, 87 (1996).
 [20] K. Freese, M. Lisanti, and C. Savage, *Rev. Mod. Phys.* **85**, 1561 (2013).
 [21] F. Mayet *et al.*, *Phys. Rep.* **627**, 1 (2016).
 [22] J. H. Jenkins and E. Fischbach, *Astropart. Phys.* **31**, 407 (2009).
 [23] J. H. Jenkins *et al.*, *Astropart. Phys.* **32**, 42 (2009).
 [24] E. Fischbach *et al.*, *Space Sci. Rev.* **145**, 285 (2009).
 [25] D. Javorsek II *et al.*, *Astropart. Phys.* **34**, 173 (2010).
 [26] P. A. Sturrock *et al.*, *Astropart. Phys.* **34**, 121 (2010).
 [27] P. A. Sturrock *et al.*, *Solar Phys.* **267**, 251 (2010).
 [28] P. A. Sturrock, E. Fischbach, and J. Jenkins, *Astrophys. J.* **794**, 42 (2014); **796**, 149(E) (2014).
 [29] P. A. Sturrock *et al.*, *Astropart. Phys.* **36**, 18 (2012).
 [30] J. H. Jenkins *et al.*, *Astropart. Phys.* **37**, 81 (2012).
 [31] P. A. Sturrock *et al.*, *Astropart. Phys.* **42**, 62 (2013).
 [32] P. A. Sturrock *et al.*, [arXiv:1907.11749](https://arxiv.org/abs/1907.11749).
 [33] A. G. Parkhomov, *J. Mod. Phys.* **2**, 1310 (2011).
 [34] S. Pomme, K. Kossert, and O. Nahle, *Solar Phys.* **292**, 162 (2017).
 [35] S. Pomme, *Eur. Phys. J. C* **79**, 73 (2019).
 [36] A. Dhaygude and S. Desai, *Eur. Phys. J. C* **80**, 96 (2020).
 [37] R. Arnold *et al.* (NEMO-3 Collaboration), *Eur. Phys. J. C* **79**, 440 (2019).
 [38] R. Arnold *et al.* (NEMO-3 Collaboration), *Phys. Rev. D* **92**, 072011 (2015).
 [39] R. Arnold *et al.* (NEMO-3 Collaboration), *Nucl. Instrum. Methods Phys. Res., Sect. A* **536**, 79 (2005).
 [40] R. Arnold *et al.* (NEMO-3 Collaboration), *Phys. Rev. D* **89**, 111101 (2014).
 [41] N. R. Lomb, *Astrophys. Space Sci.* **39**, 447 (1976).
 [42] J. D. Scargle, *Astrophys. J.* **263**, 835 (1982).
 [43] M. Zechmeister and M. Kürster, *Astron. Astrophys.* **496**, 577 (2009).
 [44] A. Milsztajn, [arXiv:hep-ph/0301252](https://arxiv.org/abs/hep-ph/0301252) v1.
 [45] J. Yoo *et al.* (Super-Kamiokande Collaboration), *Phys. Rev. D* **68**, 092002 (2003).
 [46] P. A. Sturrock, D. O. Caldwell, J. D. Scargle, and M. S. Wheatland, *Phys. Rev. D* **72**, 113004 (2005).
 [47] P. A. Sturrock *et al.*, *Astrophys. J.* **523**, L177 (1999).
 [48] B. Aharmim *et al.* (SNO Collaboration), *Phys. Rev. D* **72**, 052010 (2005).
 [49] M. Altmann *et al.* (GNO Collaboration), *Phys. Lett. B* **616**, 174 (2005).
 [50] P. Tejas and S. Desai, *Eur. Phys. J. C* **78**, 554 (2018).
 [51] Y. Nakano *et al.* (Super-Kamiokande Collaboration), *J. Phys.: Conf. Ser.* **1342**, 012037 (2020).
 [52] R. V. Baluev, *Mon. Not. R. Astron. Soc.* **385**, 1279 (2008).
 [53] J. N. Bahcall and W. H. Press, *Astrophys. J.* **370**, 730 (1991).